Magnetic-field-induced incommensurate to collinear spin order transition in $NiBr_2$

S. Babu,[1] K. Prokeš,[2, a)] Y. K. Huang,[3] F. Radu,[4] and S. K. Mishra[1, b)]

[1)] *School of Materials Science and Technology, Indian Institute of Technology, Banaras Hindu University, Varanasi-221005, India*

[2)] *Helmholtz-Zentrum für Materialien und Energie, Hahn-Meitner-Platz 1, D-14109, Germany*

[3)] *Van der Waals-Zeeman Institute, University of Amsterdam, Science Park 904, The Netherlands,*

[4)] *Helmholtz-Zentrum für Materialien und Energie, Albert-Einstein-Straße 15, D-12489, Germany*

(Dated: 27 November 2018)

The triangular spin lattice of $NiBr_2$ is a canonical example of a frustrated helimagnet that shows a temperature-driven phase transition from a collinear commensurate antiferromagnetic structure to an incommensurate spin helix on cooling. Employing neutron diffraction, bulk magnetization, and magnetic susceptibility measurements, we have studied the field-induced magnetic states of the $NiBr_2$ single crystal. Experimental findings enable us to recapitalize the driving forces of the spin spiral ordering in the triangular spin-lattice systems, in general. Neutron diffraction data confirms, at low temperature below $T_m = 22.8(1)$ K, the presence of diffraction satellites characteristic of an incommensurate magnetic state, which are symmetrically arranged around main magnetic reflections that evolve just below $T_N = 44.0(1)$ K. Interestingly, a field-induced transition from the incommensurate to commensurate spin phase has been demonstrated that enforces spin helix to restore the high temperature compensated antiferromagnetic structure. This spin reorientation can be described as a spin-flop transition in the (a–b) basal plane of a triangular spin lattice system. These findings offer a new pathway to control the spin helix in incommensurate phases that are currently considered having technical implications in the next-generation data storage devices.

[a)]Electronic mail: prokes@helmholtz-berlin.de

[b)]Electronic mail: shrawan.mst@iitbhu.ac.in

I. INTRODUCTION

Noncollinear spins are generic to the systems with spin spirals, spin helicoids, canted spins, and ferromagnetic (antiferromagnetic) domain walls. Such spin systems have attracted significant interest in recent research activities since they are potential candidates for ultra-dense magnetic storage devices [1–3]. Spin helix mainly evolve in the presence of inversion symmetry breaking and yields various unusual physical phenomena like electric excitation of magnon [4,5] and magnetic skyrmions [6,7]. Various microscopic driving mechanisms would produce noncollinear spin ordering, and among them, Dzyaloshinskii–Moriya interaction (DMI) is the most common in many systems [8,9].

Noncollinear spin arrangements in helimagnets also result from the presence of competing ferromagnetic and antiferromagnetic Heisenberg interactions between spins [10–13]. Considering exchange interactions model in a magnetic field of intensity H, the Hamiltonian **H** for a triangular lattice can be expressed through the following Eq. (1)

$$\mathbf{H} = -J_1 \Sigma_{<i,j>} S_i.S_j - J_{2,3} \Sigma_{<<i,j>>} S_i.S_j - H \Sigma_i S_i \tag{1}$$

where, $\Sigma_{<i,j>}$ and $\Sigma_{<<i,j>>}$ represent the sum over the nearest neighbor (nn) and third nearest neighbor (nnn), respectively [10]. For ferromagnetic state ($J_1 > 0$) with only nn interaction, the ground state of such system would be commensurate to the underlying lattice. However, on the other hand, for competing interactions such as $J_1 > 0$ and the AF third-neighbor interaction $J_3 < 0$, an incommensurate ground state is more favorable [10,14–17].

Transition metal dihalides have long been considered as prototypes of antiferromagnets with a triangular lattice [18–20,22–24]. Most of the privious investigations on dihalides were focused on the coupling between magnetism and ferroelectricity [19,20]. $NiBr_2$, an archetypal dihalides displays a paramagnetic-antiferromagnetic phase transition at $T_N = 44.0(1)$ K and then antiferromagnetic-incommensurate spiral transition at $T_m = 22.8(1)$ K [22–24]. The ground state of the incommensurate spiral exhibits a threefold degeneracy with respect to the three equivalent wave vectors of the lattice. This threefold degeneracy is predicted to be a source of various distinctive ordered states, namely, multiple-q state [25]. The multiple-q state can also results skyrmionic state in such system, as proposed theoretically by Okubo et al. [25].

In this work, we have revisited the various characteristics of the incommensurate helix phase in the single crystal $NiBr_2$ using dc(ac) magnetization and magnetic susceptibilities, neutron diffraction, and small angle neutron scattering. The experimental findings suggest that $NiBr_2$ has an incommensurate spiral ground state corrobarating previous investigations [19,20,22,23]. We observed that the system responds to the structural symmetry of 120° by populating the three equivalent wave vectors in the incommensurate state. In this report, we emphasize on a magnetic-field-induced spin reorinetation from the incommensurate spiral to collinear commensurate phase.

II. METHODS AND EXPERIMENTAL DETAILS

High-quality single crystals of $NiBr_2$ were grown at the University of Amsterdam, using a self-flux growth method starting from a stoichiometric mixture of Ni, and Br, as reported in Tokunaga et al. and Kurumaji et al. [19–21].$NiBr_2$ crystal forms naturally layered shape with the c-axis perpendicular to planes that efficiently cleave. The nickel ions occupy a single site in the Bravais lattice as shown in Fig. 1(a). Magnetic measurements at various temperatures ranging across 2-300 K were carried out using the MPMS 7T device and PPMS 14T (Quantum Design) systems, in fields up to 14 T, which applied within and perpendular of the basal plane .

Neutron diffraction experiments were carried out on the diffractometers E2, E4 and the small-angle neutron scattering instrument V4 at the BER II reactor of the Helmholtz-Zentrum Berlin (HZB) [26]. In the part, magnetic fields up to 5 T were applied along and perpendicular to the trigonal axis of the single-crystalline $NiBr_2$ using a horizontal-field cryomagnet that restricts significantly the scattering geometry. E2 and E4 instruments use a pyrolytic graphite (002) monochromator selecting the neutron wavelength $\lambda = 2.4$ Å. The data were collected with two-dimensional position sensitive ^{3}He detectors that were of different sizes at respective instruments. $\frac{\lambda}{2}$ filters were used at both E2 and E4 instruments imply residual higher-order wavelength contamination at a level of less than 10^{-4}. In addition, the small-angle neutron scattering measurements were carried out with instrument V4 that possess a large position-sensitive detector movable at the distance between 1 and 16 m from the sample. In order to refine the magnetic structure of $NiBr_2$, we have collected data mainly in the (hhl) plane.

The crystal and magnetic structure refinements were performed with the program Fullprof [27,28]. The nuclear scattering lengths b(Ni) = 1.03 fm and b(Br) = 0.6795 fm were considered. For the absorption correction (Gaussian integration), we used the absorption coefficient $\mu = 0.12\,\mathrm{cm}^{-1}$. No secondary extinction correction has been applied.

III. RESULTS AND DISCUSSIONS

A. Magnetization and Susceptibility

Figure 2(a) illustrates the temperature dependence of the magnetic susceptibility $\chi = M/H$ of $NiBr_2$, where, the M is magnetization, and the H is magnetic field ranging between 1.0 and 14.0 T, which was applied perpendicular to the c-axis. In the case of $NiBr_2$ at high temperatures where $\chi = M/H$ measured the magnetization is directly proportional to the applied magnetic field (i.e. linear in the field), the evaluated M/H values are identical to the magnetic susceptibility at different fields are insensitive to the magnetic field strengths.

At lower temperatures, two well-distinguished anomalies can be discerned marking the magnetic phase transition temperature that were determined from maxima of $\frac{\partial T.\chi(T)}{\partial T}$. At H = 1.0 T, the transition between the paramagnetic and an antiferromagnetic state is detected at $T_N = 44.6(1)$ K. A closer inspection reveals that for increasing the magnetic field the transition shifts toward lower temperatures. The second transition between antiferromagnetic to helical spin ordering takes place at $T_m = 21.8$ (1) K. As shown in Fig. 2(a), this transition also shifts toward lower temperatures as a function of the magnetic field.

The temperature dependence of $1/\chi(T)$ and their fits with a modified Curie–Weiss law are shown in inset panels of Fig. 2(a and b). The modified Curie–Weiss law can be expressed by Eq.(2):

$$\chi = C/(T - \theta_p) + \chi_0 \tag{2}$$

where, C represents the Curie constant and θ_p the paramagnetic Curie temperature. χ_0 denotes the temperature-independent terms. The excellent quality of fits confirm the modified Curie-Weiss behavior for the system above $T > 70$ K. The best fit of data acquired with 1.0 T ($T > 150$ K) yields the effective moment of $\mu_{eff} = 2.76$ (1) μ_B. This value is approximately the same as the effective moment expected for the S = 1, $3d^8$ electronic configuration of Ni ions ($\sqrt{8} = 2.83$). The effective moment determined from data taken at 14.0 T amounts to

2.66 (1)μ_B. The fitted values of θ_p amount to 22.2(1) K and 28.1 (1) K for the data recorded 1.0 T and 14.0 T, respectively.

Figure 2(b) shows the temperature dependence of magnetic susceptibility measured for the various field applied along the c-axis. In this orientation, the magnetic susceptibility at higher temperatures is field independent with anomalies at the lower temperatures. The effective magnetic moment and the paramagnetic Curie temperature are very similar to the privious orientation (μ_{eff} =2.74 (1)μ_B and θ_p = 21.3 (1) K, respectively). The best fit to data taken at 14 T applied along the c-axis is shown in the inset of Fig. 2(b).

For $T > 70$ K, the similarity between magnetic susceptibilities with field applied along and perpendicular to the c-axis suggests that the anisotropy in paramagnetic state of $NiBr_2$ is negligible. However, this does not hold true for the state below T_N as magnetization (M–H) curves taken for field applied perpendicular and along the c-axis had shown entirely different magnetization behaviors, as depicted in Fig. 3(a and b). For the case when applied magnetic field within the (a–b) basal plane, a clear field-induced transition noticed that shifts to a lower field upon increasing temperature. At T=3 K, the magnetization step associated with the transition amounts to about 0.036 μ_B/Ni. This is in good agreement with the magnetic susceptibility data.

Now, we discuss the insights of such phase transitions through measurements of the temperature and magnetic field dependence of ac magnetic susceptibility, which is a complex value and expressed as $\chi_{ac} = \chi' - i\chi''$. The real component, χ', is related to the reversible magnetization process and always in-phase with the oscillating field. However, imaginary component, χ'', is related to losses during the irreversible magnetization process. The measurements of ac susceptibilities were carried out for multiple values of applied fields as a function of temperature (measured with H = 1 mT and f = 99 Hz). To minimize the demagnetization effects, the dc magnetic fields were applied within the basal plane (a–b). Fig. 4(a) illustrates the temperature dependence of the ac susceptibilities measured in the vicinity of both transitions. Experimental results over the field range from 0.1 to 2.0 T show the emergence of a maxima across both phase transitions. Over the T_m, ac susceptibility displays a maxima with respect to the temperature; the position of which trending towards higher side (while the amplitude of ac susceptibility decreases) with reducing the strength of applied magnetic fields, similar as in Ref. [20]. The variation in peak heights and temperatures for various dc magnetic fields shows a monotonic variation with strength of the

applied dc field.

Figure 4(b) shows the ac susceptibilities as a function of applied magnetic fields for various constant temperatures ranging across 5-80 K. At $T = 80$ K, the ac susceptibility exhibits a line-shaped curve with low amplitude. At $T = 25$ K; a peak can be seen close to the upper phase boundary of the antiferromagnet state as also seen in Fig. 2(a). At even lower temperature near T=20 K, an increase in ac susceptibility peak amplitude is clearly noticed for applied low fields 0.5 T $<$ H $<$ 2.5 T. This modified ac susceptibility magnitude is also accompanied by a systematic enhancement in the peak field, which would correspond to the boundary of incommensurate phase in this region. Repeating the field dependence of ac susceptibilities at various temperatures across incommensurate phase result a χ(H,T) curve as illustrated in Figure 4(b). Below $T_{\rm m}$, a hysteresis nature of χ(H,T) curves clearly evident, which acquired for different temperatures, confirming the helix nature of noncollinear spins. The shift in peak positions as a function magnetic field represent the torque required to reverse the helical spin upon flipping the polarization of applied magnetic field. The results reported above indicate the emergence of incommensurate to commensurate phase transition (as demonstrated further below by neutron scattering), a generic response that occurs only across the low temperature boundary of these phases. The ac susceptibility peak positions in (H,T) dimensions over the typical ranges map directly onto the field-induced modulation in incommensurate phase. It should be noted that at zero field, ac susceptibility diminishes monotonically over the range of temperatures between 5–20 K.

B. Neutron diffraction on $NiBr_2$ crystal

$NiBr_2$ crystallizes in the $CdCl_2$ structure, which has the rhombohedral space group D^5_{3d} [18–20,22,23]. The Ni and Br atoms are situated at the Wyckoff positions $3a$(0,0,0) and $6c$(0,0,z) with 3 m and -3 m local symmetries, respectively [22,23]. The lattice constants are a = 3.723 Å and c = 18.340 Å. The space group leads to specific extinction conditions, for instance, the reflections $hkil$: $-h+k+l = 3n$ and the reflections $hki0$: $-h+k = 3n$.

Figure 5(a) illustrates the (hhl) diffraction pattern recorded at 50 K. As it is evident that only (110), (003), (006), and (009) Bragg reflections are observed (along with signal originating from the Al-sample holder/cryostat)[22,23]. The refinement of observed Bragg reflections leads to a reasonable agreement with literature data. For $T_{\rm N} <$ T $< T_{\rm m}$, new

Bragg reflections associated with AF order are observed that have been indexed with a propagation vector q_c = (0 0 3/2) (see Fig. 5(b)). The diffraction pattern recorded at 26 K confirms that (0 0 3/2), (0 0 9/2), and (0 0 15/2) are magnetic satellites corroborating the antiferromagnetic ordering of Ni spins in (a–b) basal plane [22,23,26,29].

To record the tiny incommensurate components, we have utilized high wavelength neutrons with λ = 2.4 Å produced by a pyrolytic graphite monochromator. Graphite filters were used to remove the $\lambda/2$ contamination. The signal to noise ratio were optimized by varying the slits opening [26,29]. The component of propagation vector along the c-axis remains commensurate with a value $k_z = 3/2$. However, an incommensurate component exists in the (a–b) basal plane, which is oriented along $<$ 110 $>$ direction. For the temeprature ranging between 4.2-21.8 K the propagation vector has been found to be temperature dependent. The absence of any higher harmonics (Fig. 5(c)) proves that $NiBr_2$ orders with a helical structure within the (a–b) basal plane in zero field at T = 2 K.

Upon applying an in-plane magnetic field (H $\leq$ 4 T), the magnetic satellites regain its shape similar to commensurate antiferromagnetic as shown in Fig. 5(d). This transition of magnetic satellite peaks are manifested in incommensurate phase. A significant change in the diffraction patterns reported at T=21.1K, as the q_c Bragg reflections split (see Fig. 5(c)). The estimated propagation is of the q_i = (q_h q_h 3/2), with $q_h \approx 0.03$. Figure 5(d) shows the pattern recorded at 2 K and 4 T. As can be seen, an identical diffraction pattern recorded at 26 K (see Fig. 5(b)). At T= 50 K, one can also notice a detectable short-range ordered signal. Such field-induced spin reorientation in single crystal of incommensurate $NiBr_2$ is observed with a magnetic field applied perpendicular to c-axis. For critical field (H $\geq$ 4 T) and temperature ranging across 4.2-22 K, a complete spin reorientation has been observed. This finding will be further examined within the framework of spin-flop coupling in the upcoming sections.

Figure 6 shows the temperature dependence of the magnetic (0 0 3/2) Bragg reflection recorded with zero field upon cooling at the top of the reflection. The solid red line represents the best fit of the experimental data using Eq.(3):

$$I(T) = b + I_0(1 - \frac{T}{T_N})^{2\beta} \tag{3}$$

where, b denotes the background intensity, I_0 represents the intensity at 0 K, and β is the critical parameter related to dimensionality of the system. The best fit to this empirical

formula, which is valid in the critical region near the magnetic phase transition, leads to a good description of the data above 40 K. The magnetic phase transition occurs at T_N = 44.5 (6) K with β = 0.30 (1). However, the observation of scattered intensity (see the non-negligible intensity above the background level in the Fig. 6 highlighted by the dashed line) above the T_N points to the presence of critical scattering in this material. The second-order transition at T_m takes place at 21.6 (5) K. As it is shown in Fig. 6, the intensity originates from new Bragg reflections that contribute to the original (0 0 3/2) Bragg reflection.

Figure 7(a) shows diffraction pattern recorded at 2 K with zero magnetic field around the (0 0 3/2) reciprocal space position, using projection on the $\omega-\upsilon$ plane, where ω is the rotational angle of the sample, and υ is the deviation angle from the scattering plane. As it is evident, the original magnetic Bragg reflection splits into six reflections indexed by three propagation vectors $q_1 = (q_h\, q_h\, 3/2)$, $q_2 = (\text{-}q_h\, 2q_h\, 3/2)$, and $q_3 = (\text{-}2q_h\, q_h\, 3/2)$ (and associated opposite vectors). Using the UB matrix refined from very few nuclear Bragg reflections and positions of the maxima, it follows that q_h = 0.027 (1) is in agreement with the literature [30,31]. The six magnetic reflections can be indexed as (−0.027 −0.027 3/2), (−0.054 0.027 3/2), (−0.027 0.054 3/2), (0.027 0.027 3/2), (0.054 −0.027 3/2) and (0.027 −0.054 3/2). These propagation vectors are incommensurate with the crystal structure. The projection of Fig. 7(a) on the rotational axis, ω is shown in Fig. 7(b), suggesting that these reflections have inhomogeneous intensity distributions.

The existence of six magnetic propagation vectors at low temperatures can results only in the two diffrent situations. In the first case, a homogeneous state where the Ni magnetic moments are modulated in the entire sample by all three propagation vectors. In second case, a spatially disjoint domains that can be populated by each having one propagation vector at a time. Experimentally the reflection described by the propagation vector q_3 is by about 50 % more intense than the $-q_2$ reflection (see Fig. 7(a)), the first scenario can be ruled out. This confirms that the magnetic structure consists of volume-separated domains confirming incommensurate phase with three equivalent directions of wave vectors.

Figure 8(a) shows the temperature dependence of the diffracted intensities projected on the ω-axis along with projections on the $\omega-\upsilon$ plane (Fig. 8(b)) recorded at various temperatures. As clearly visible that incommensurate reflections collapse at T_m to a single (0 0 3/2) reflection. The absence of any anomaly around T_N suggests that the (0 0 3/2) reflection just splits into six reflections at lower temperature without any significant change

in magnetic moment magnitude.

Symmetry analysis for commensurate and incommensurate types of propagation vectors leads to conclusion that Ni magnetic moments can either oriented along or perpendicular to the c-axis. However, non-zero intensities at (0 0 3/2) position suggests that the moments are oriented within the (a–b) basal plane. The best fit to data shown in Fig. 5(b), i.e., data taken in zero fields at 25 K, leads to Ni moment magnitude of 2.8 (2) μ_B. This value is somewhat larger than the reported in the privious investigations [22,23]. It is important to mention that there could other feasible magnetic structures that also can agree equally with the experimental data. Fig. 9(a and b) shows the two such solutions with collinear alignment of Ni moments. The best fit to data taken at 2 K, 0 T as shown in Fig. 5(c) using six propagation vectors q_1 = (−0.027 −0.027 3/2), q_2 = (−0.054 0.027 3/2), q_3 = (−0.027 0.054 3/2), q_4 = (0.027 0.027 3/2), q_5 = (0.054 −0.027 3/2), and q_6 = (0.027 −0.054 3/2) leads to Ni magnetic moment of 3.0 (3) μ_B. The direction of Ni moments has been changing within the basal plane in an incommensurate manner, making with respect to each other about $\alpha = 9.5°$ as one moves within the plane along a-axis as illustrated in Fig. 9(c). This solution is in good agreement with the literature [22–24]. The population of six magnetic domains is about 18%:10%:22%:13%:19%:18%.

Now, we would elaborate in more detail about the spin-flop mechanism across the incommensurate phase that is induced in the presence of an external magnetic field (H $\geq$ 4 T) applied within the (a–b) plane. In Fig. 10(a), the temperature dependence of the intensity around (0 0 3/2) position is measured with increasing temperature in a field of 2 T applied within the (a–b) plane. As the magnitude of applied field increases above the critical field, only the magnetic reflections indexable with q_c = (0 0 3/2) are present. Fig. 10(b) shows the temperature dependence of the intensity around (0 0 3/2) position measured with increasing temperature with magnetic field of 5 T applied within the (a–b) plane. The high temperature magnetic phase is retained as shown in Fig. 10(b) that display the field dependence of the intensity projected on ω-axis. In the presence of weak anisotropic energy, at a critical magnetic field this phase transition can be interpreted as the two sub-lattice magnetization rotates suddenly to a direction perpendicular to easy axis.

C. Phase diagram

The magnetic phase diagram of $NiBr_2$ near critical temperature $T_m(T_N)$ has been drawn from the measurements of bulk magnetization, susceptibility, and neutron diffraction. A decrease of the magnetic phase boundary at T_N results in a substantial increase of the satellite q-vector. As shown in the Fig. 11, for an intermediate temperature range in the (a–b) plane, a commensurate magnetic structure between 45 K and 22 K was found by a least-squares refinement to be modulated with moments lying in the (a–b) plane. At lower temperatures and moderate magnetic field in the (a–b) plane, an incommensurate magnetic structure between 22 K and 4 K was found by a least-squares refinement to be modulated with moments lying in the (a–b) plane with angle of $\gamma = 9.6^\circ$. The inset shows the extended field range that suggests for the field applied within the (a–b) plane, yet another field-induced transition around 60 T.

This behavior in $\chi(H,T)$ may be a defining characteristic of such transitions, mainly reflecting the unusual combination of ferromagnetic and antiferromagnetic interactions in the $NiBr_2$ system that leads to the complicated influence of applied fields on the changing spin configurations along the commensurate-incommensurate boundary. As Rastelli et al. [14] predicted, when J_{nn} and J_{nnn} are both positive, the lattice is ferromagnetic, but when either or both are negative, helical or antiferromagnetic. The helical magnetic structure found in $NiBr_2$ at low temperature results from a very delicate and fortuitous balance of the various J_i. Elevated temperature forces the system across boundary from incommensurate to commensurate phase. The interplay between competing interactions lead to amplitude-modulated magnetic structure having a periodicity that do not match with crystal lattice [32–35].

D. SUMMARY AND CONCLUSIONS

By magnetic measurements and neutron diffraction of $NiBr_2$, we demonstrated a systematic variation of exchange interactions and helical wave vector as a function of the applied magnetic field. The changes we noticed in the magnetic properties are dominated by the variation of anisotropy and exchange interactions. We also demonstrated a magnetic field-induced phase transition across the incommensurate phase, which entirely transform

the low-temperature incommensurate phase into the high temperature commensurate spin structure. This behavior of incommensurate phase is purely governed by spin-flop transition. On the methodological side, our work demonstrates that combining state-of-the-art neutron scattering experiments with magnetization measurements, we were enable to extract definitive microscopic information from the spin triangular system of $NiBr_2$. These findings accelerate the search for exotic quantum states in helimagnetic systems through the screening of many related materials having direct technological implications.

ACKNOWLEDGMENTS

Authors thank M. Reehuis, F. Yokaichiya and U. Keiderling for technical help with the neutron data collection. We would like to acknowledge CIFC, IIT (BHU) for the magnetic measurements. SKM acknowledges the funding from the IIT(BHU) with grant no. IIT(BHU)/R&D/SM/2016-17/4453.

REFERENCES

[1]A. Fert, V. Cros, and J. Sampiao, Nat. Nanotech. **8**, 152156 (2013).

[2]J. Sampaio, V. Cros, S. Rohart, A. Thiaville, and A. Fert, Nat. Nanotech. **8**, 839844 (2013).

[3]S. Emori, U. Bauer, S.-M. Ahn, E. Martinez, and G. S. D. Beach, Nat. Mater. **12**, 611616 (2013).

[4]T. Kimura, J. C. Lashley, and A. P. Ramirez, Phys. Rev. B **73**, 220401(R) (2006).

[5]S. Seki, N. Kida, S. Kumakura, R. Shimano, and Y. Tokura, Phys. Rev. Lett. **105**, 097207 (2010).

[6]S. Muhlbauer, B. Binz, F. Jonietz, C. Pfleiderer, A. Rosch, A Neubauer, R. Georgii, and P. Boni, Science **323**, 915-919 (2009).

[7]U. K. Rossler, A.N. Bogdanov, and C. Pfleiderer, Nature Lett. **442**, 797-801 (2006).

[8]I. Dzyaloshinskii, J. Phys. Chem. Solids **4**, 241-255 (1958).

[9]T. Moriya, Phys. Rev. Lett. **4**, 228 (1960).

[10]M. Azhar, and M. Mostovoy, Phys. Rev. Lett. **118**, 027203 (2017).

[11]T. Masuda, A. Zheludev, A. Bush, M. Markina, and A. Vasiliev, Phys. Rev. Lett. **92**, 177201 (2004).

[12]R Zinke, J Richter, and S-L Drechsler, J. Phys.: Condens. Matter, **22**, 446002 (2010).

[13]J.Villain, Physica B+C, 86-88B, 631-633 (1977).

[14]E. Rastelli, A. Tassi, L. Reatto, Physica B+C, **97**, 1-24 (1979).

[15]F. Ye, J. A. Fernandez-Baca, R. S. Fishman, Y. Ren, H. J. Kang, Y. Qiu, and T. Kimura, Phys. Rev. Lett. **99**, 157201 (2007).

[16]J. T. Haraldsen, M. Swanson, G. Alvarez, and R. S. Fishman, Phys. Rev. Lett. **102**, 237204 (2009).

[17]Randy S. Fishman and Satoshi Okamoto, Phys. Rev. B **81**, 020402(R) (2010).

[18]R. J. Pollard, V. H. McCann, and J. B. Ward, J. Phys. C **15**, 0022-3719 (1982).

[19]Y. Tokunaga, D. Okuyama, T. Kurumaji, T. Arima, H. Nakao, Y. Murakami, Y. Taguchi, and Y. Tokura, Phys. Rev. B **84**, 060406(R) (2011).

[20]T. Kurumaji, S. Seki, S. Ishiwata, H. Murakawa, Y. Tokunaga, Y. Kaneko, and Y. Tokura, Phys. Rev. Lett. **106**, 167206 (2011).

[21]E. N. Sickafus and D. R. Winder, J. Appl. Phys. **35**, 2541 (1964).

[22]P. Day, A. Dinsdale, E. R. Krausz, and D. J. Robbins, J. Phys. C **9**, 2481 (1976). P. Day, and K. R. A. Ziebeck, J. Phys. C **13**, L523 (1980).

[23]A. Adam, D. Billerey, C. Terrier, R. Mainard, L. P. Regnault, J. Rossat-Mignod, and P. Meriel, Solid State Commun. **35**, 1-5 (1980).

[24]L.P. Regnault, J. Rossat-Mignod, A. Adam, D. Billerey, and C. Terrier, J. Phys. France **43**, 1283-1290 (1982).

[25]Tsuyoshi Okubo, Sungki Chung, and Hikaru Kawamura, Phys. Rev. Lett. **108**, 017206 (2012).

[26]K. Prokes and F. Yokoachiya, **3**, (2017) A104 (2017).

[27]T. Roisnel, and J. Rodrguez-Carvajal,**378**, 118 (2001).

[28]V. F. Sears, *International Tables of Crystallography* vol. C, ed. A. J. C. Wilson (Kluwer, Dordrecht, 1992) 383.

[29]C. Stock, S. Jonas, C. Broholm, S. Nakatsuji, Y. Nambu, K. Onuma, Y. Maeno, and J.-H. Chung, Phys. Rev. Lett. **105**, 037402 (2010).

[30]D.I. Svergun, and L.A. Feigin, Editted by G. W. Taylor, (1987) *Structure Analysis by Small-Angle X-ray and NeutronScattering*. Plenum Press, New York.

[31]A. S. Cameron, Y. V. Tymoshenko, P. Y. Portnichenko, J. Gavilano, V. Tsurkan, V. Felea, A. Loidl, S. Zherlitsyn, J. Wosnitza, D. S. Inosov, J. Phys. Condens. Matter **28**, (146001 (2016).

[32]R. J. Birgeneau, J. Skalyo, and G. Shirane, J. Appl. Phys. **41**, 1303 (2003).

[33]Noriki Terada, Setsuo Mitsuda, Toru Fujii, Kenichiro Soejima, Ikuo Doi, Hiroko Aruga Katori, and Yukio Noda, J. Phys. Soc. Jpn. **74**, 2604-2611 (2005).

[34]F. Heidrich-Meisner, A. Honecker, and T. Vekua, Phys. Rev. B **74**, 020403(R) (2006).

[35]Randy S. Fishman, Phys. Rev. Lett. **106**, 037206 (2011).

Figure Captions

FIG. 1. (Color online) (a) Schematic representation of the crystal structure of $NiBr_2$. Green and accent small spheres represent Ni and Br ions in a layered triangular lattice, respectively. a, b and c are the principal axes of the hexagonal cell where c is the high-symmetry axis. (b) and (c) depict the collinear antiferromagnetic (AF) ($T_m < T < T_N$) and helical spin ($T < T_m$) structures, respectively. Solid arrows indicate spin directions on Ni^{2+} ions. For simplicity, bromide ions are not shown.

FIG. 2. (Color online) Temperature dependence of the magnetic susceptibility of $NiBr_2$ measured with field was applied parallel to (a) (a–b) basal plane and (b) along the c-axis, respectively. The insets show the temperature dependence of the inverse magnetic susceptibility $1/\chi(T)$ measured at 14 T in both respective panels.The red solid line is the best fit of $1/\chi(T)$ to a modified Curie–Weiss law.

FIG. 3. (Color online)(a) Field dependence of the $NiBr_2$ magnetization applied perpendicular to the c-axis for various temperatures. The full field range ($\pm$ 14 T) of M–H curves are shown in the inset. (b) Field dependence of the $NiBr_2$ magnetization applied along the c-axis measured at various representative temperatures between 3 K and 60 K.

FIG. 4. (Color online) (a) The temperature dependence of the ac susceptibility, χ(H,T) of $NiBr_2$ in the vicinity of the lower transition(s), near 50 K, measured in various static applied fields between 0.1 and 2.0 T. Isothermal ac susceptibility χ(H,T) measured over the range $5\ K \leq T \leq 80\ K$, $0.0 \leq H \leq 3.0T$. (b) The hysteresis regime Fig. 4(b) corresponds to the incommensurate phase, $5\ K \leq T \leq 25\ K$. For higher temperature $25\ K \leq T \leq 80K$, χ(H,T) shows a straight line confirming the compensated antiferromagnetic phase area.

FIG. 5. (Color online) Diffraction patterns of the $NiBr_2$ single crystal in the (*hhl*) plane at mentioned conditions: (a) 50 K, 0 T, (b) 26 K, 0 T, (c) 2 K, 0 T and (d) 2 K, 4 T applied within the (*a*–*b*) basal plan. Insets show the highlighted area around the (0 0 3/2) reciprocal space.

FIG. 6. (Color online) The temperature dependence of the magnetic (0 0 3/2) Bragg reflection measured upon cooling at the top of the reflection. The solid line through the points just below the T_N is the best fit to the Eq. (4) given in the text. The second-order transition at T_m takes place at 21.6 (5) K. Just above the T_N, a magnetic diffraction signal due to short-range correlations is visible, which is highlighted with a dashed line.

FIG. 7. (Color online) (a) The diffraction pattern recorded with zero field around the (0 0 3/2) magnetic reflections in reciprocal space using $\omega-\upsilon$ projection. (b) The conventional projection of diffraction pattern on the rotational ω-axis.

FIG. 8. (Color online) (a and b) The temperature dependence of the diffracted signal around the magnetic (0 0 3/2) Bragg reflection projected on the ω-axis along with detection as seen on the 2D detector on E4 at various temperatures in zero field.

FIG. 9. (Color online) Schematic representation of AF structure of $NiBr_2$ at 26 K, 0T (a) and 2 K , 0 T (b). (c) A possible solution that agrees with data taken at 26 K, 0T equally well. Only Ni atoms are shown. In all cases, $2 \times 2 \times 1$ crystallographic unit cells are shown. The moments in underlying cell along the *c*-axis are reverted.

FIG. 10. (Color online) (a) Temperature dependence of the intensity around the (0 0 3/2) measured with field of 2 T applied within the (*a*–*b*) plane. (b) Temperature dependence of the intensity around the (0 0 3/2) measured with field of 5 T applied within the (*a*–*b*) plane.

FIG. 11. (Color online) Magnetic phase diagram of $NiBr_2$ constructed from magnetic bulk measurements (circles and squares) and neutron diffraction data (stars). In the inset, a crude estimate of the critical field associated with the T_N is represented. The dotted line is a guide for an eye.

Figure 1

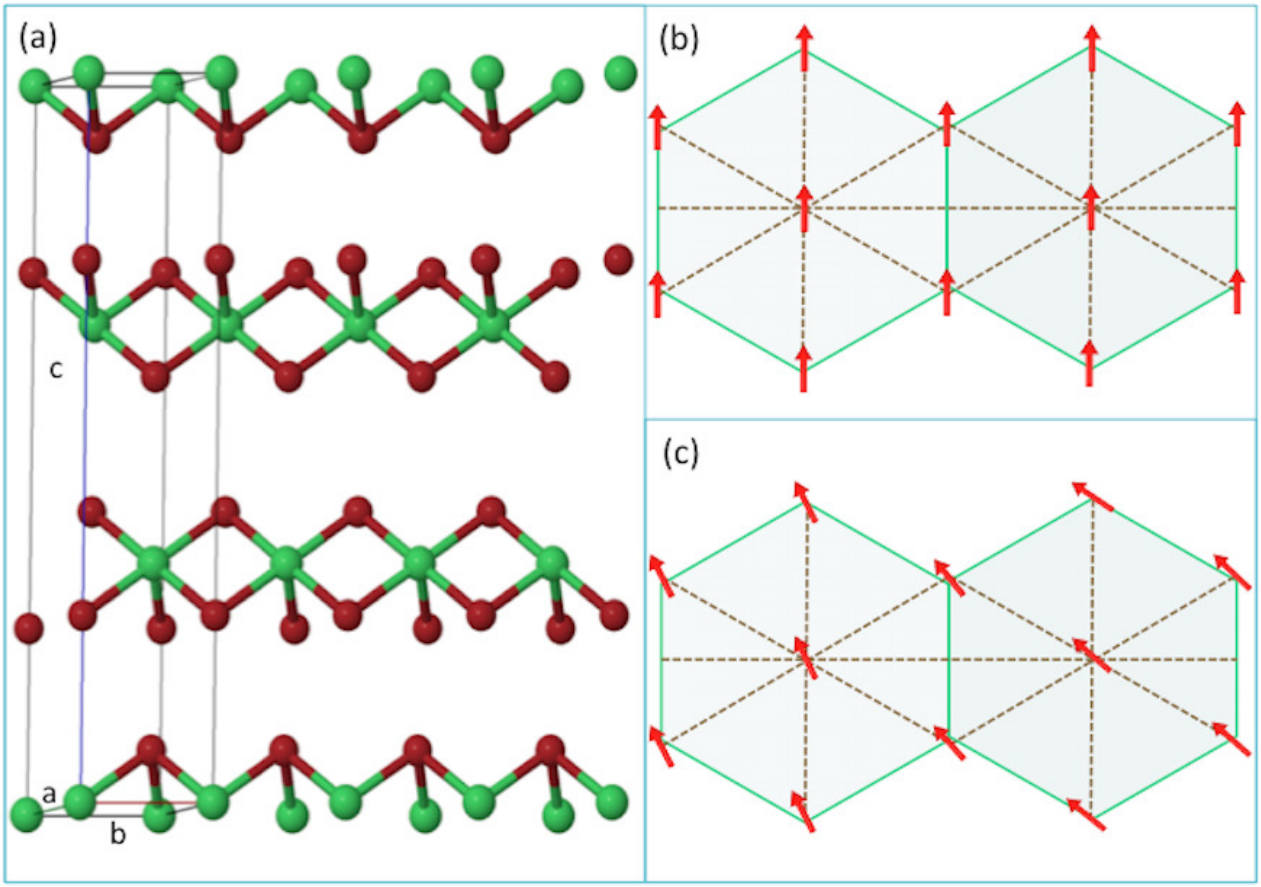

Figure 2

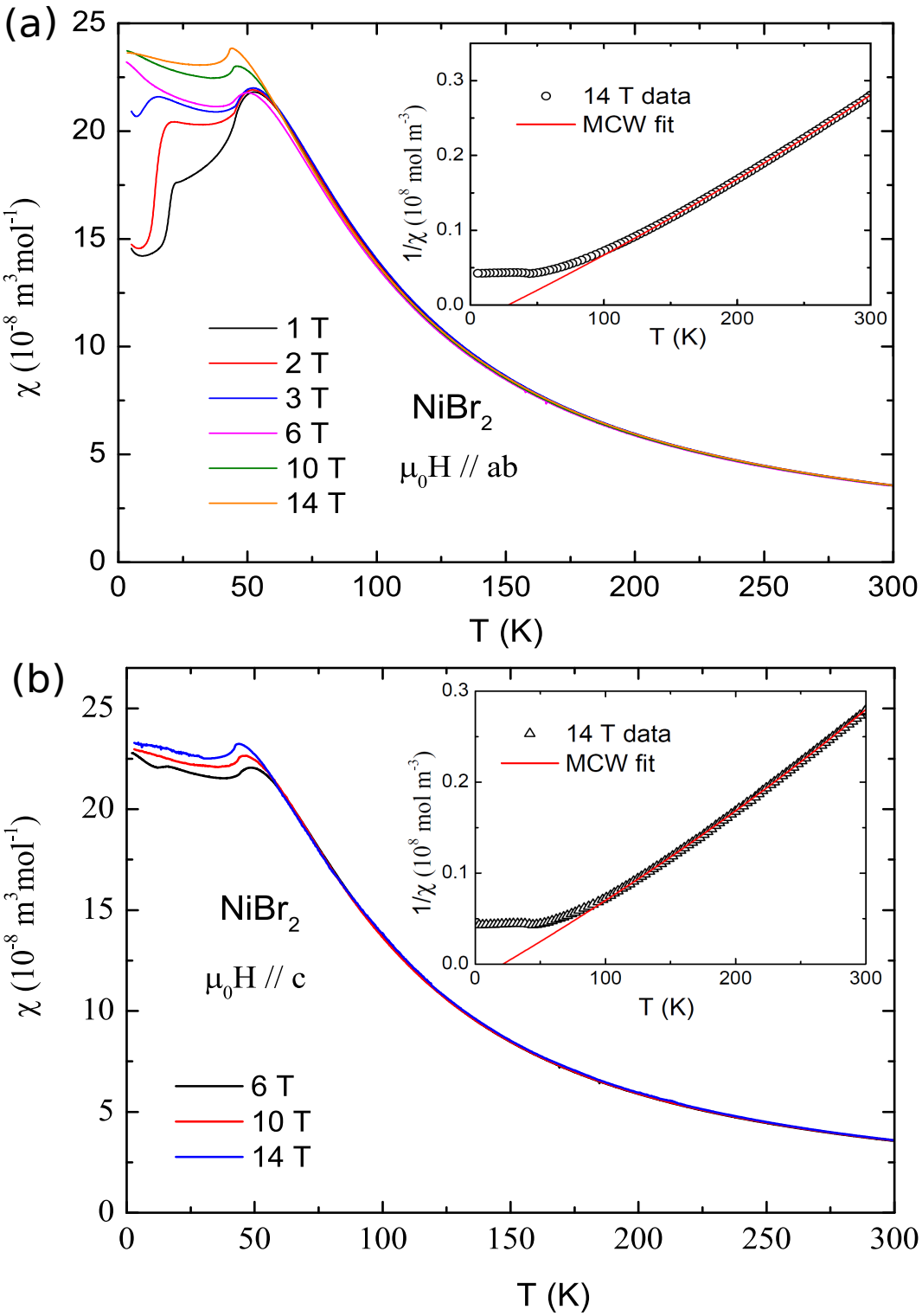
(a)
χ (10^-8 m^3 mol^-1)
T (K)
1 T
2 T
3 T
6 T
10 T
14 T
NiBr2
μ0H // ab
1/χ (10^8 mol m^-3)
14 T data
MCW fit
(b)
χ (10^-8 m^3 mol^-1)
T (K)
6 T
10 T
14 T
NiBr2
μ0H // c
1/χ (10^8 mol m^-3)
14 T data
MCW fit

Figure 3

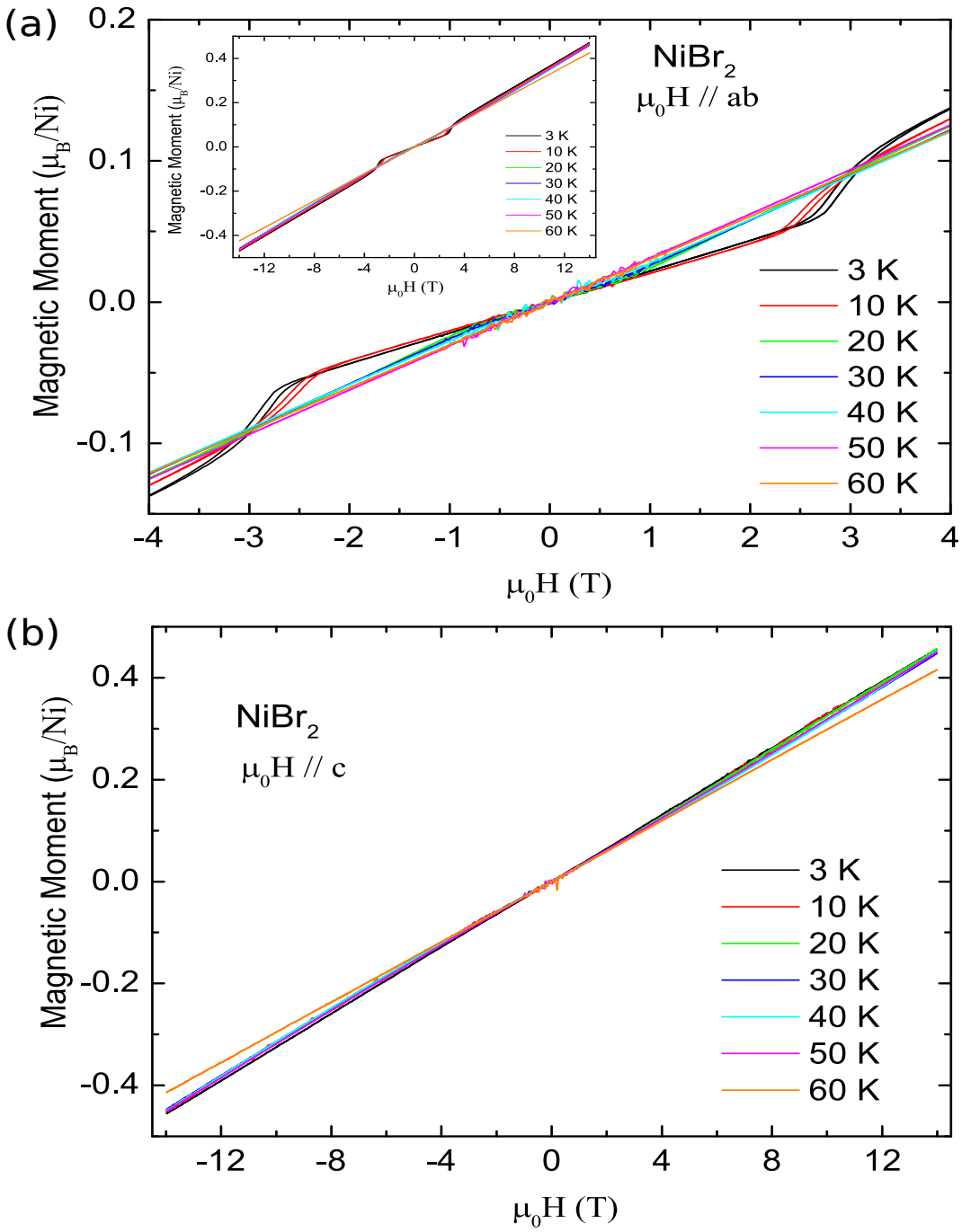
(a)
NiBr2
μ0H // ab
Magnetic Moment (μB/Ni)
μ0H (T)
3 K
10 K
20 K
30 K
40 K
50 K
60 K
(b)
NiBr2
μ0H // c
Magnetic Moment (μB/Ni)
μ0H (T)
3 K
10 K
20 K
30 K
40 K
50 K
60 K

Figure 4

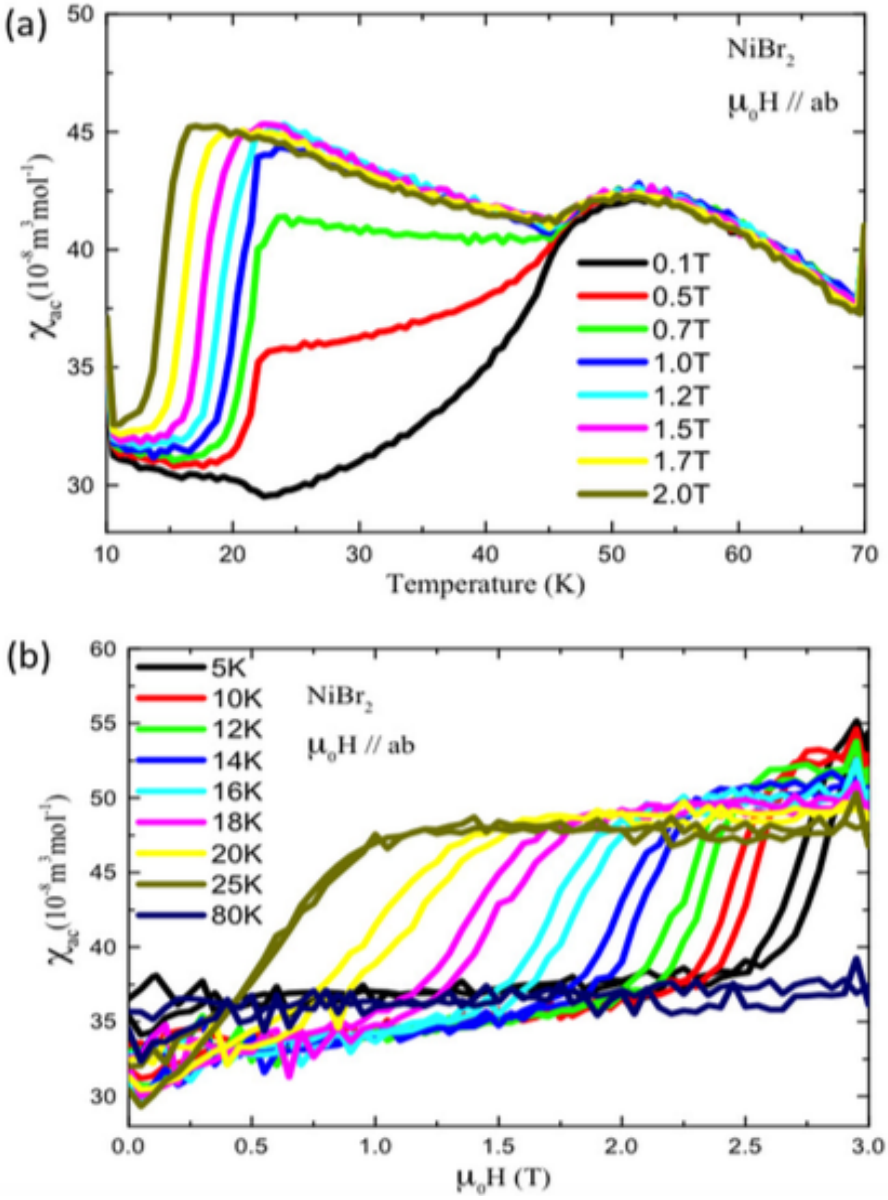
(a)
NiBr2
μ0H // ab
0.1T
0.5T
0.7T
1.0T
1.2T
1.5T
1.7T
2.0T
χac(10-8m3mol-1)
Temperature (K)
(b)
5K
10K
12K
14K
16K
18K
20K
25K
80K
NiBr2
μ0H // ab
χac(10-8m3mol-1)
μ0H (T)

Figure 5

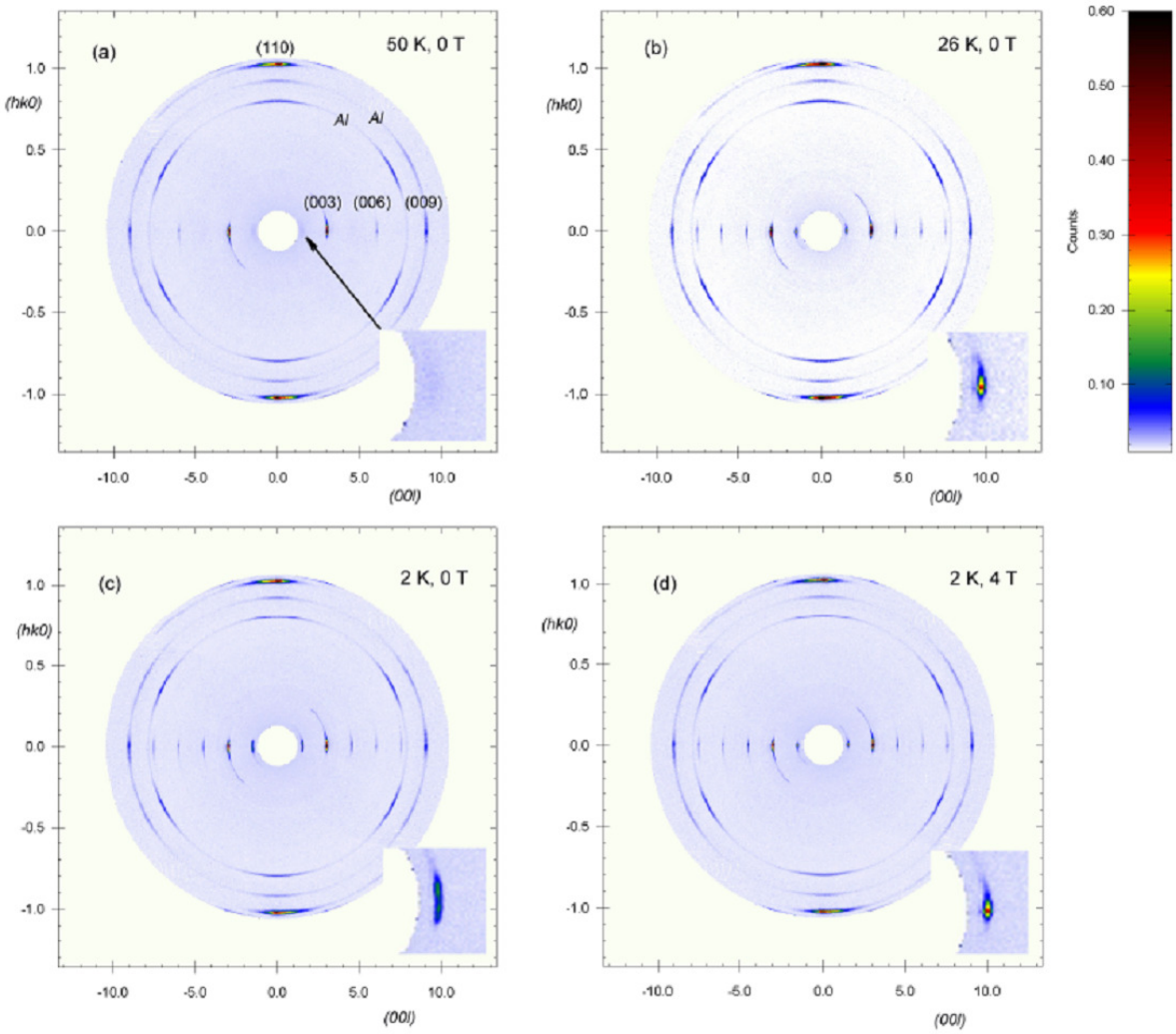
(a)
50 K, 0 T
(110)
Al
Al
(003)
(006)
(009)
(b)
26 K, 0 T
(c)
2 K, 0 T
(d)
2 K, 4 T
(hk0)
(00l)
Counts
0.60
0.50
0.40
0.30
0.20
0.10

Figure 6

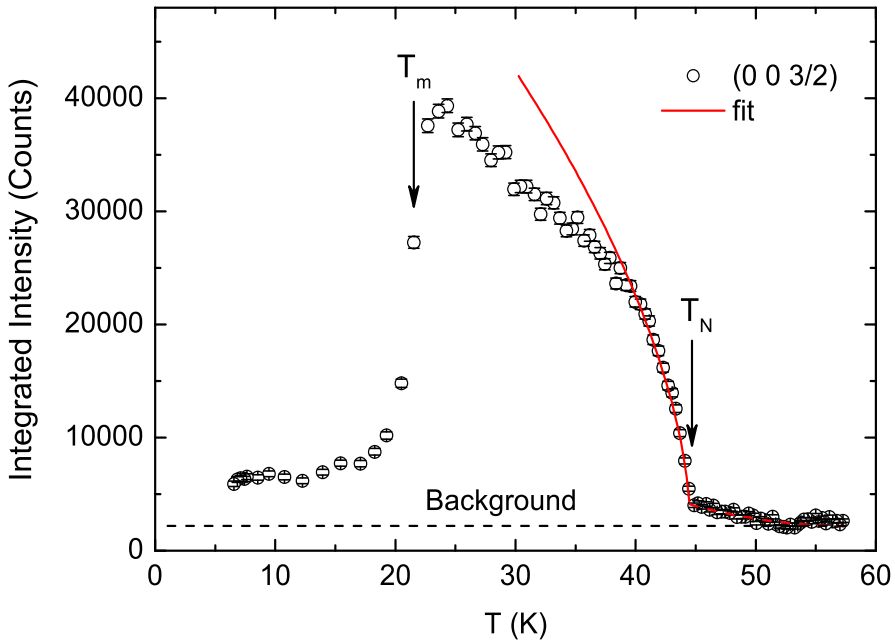
Integrated Intensity (Counts)
T (K)
T_m
T_N
(0 0 3/2)
fit
Background
0
10000
20000
30000
40000
0
10
20
30
40
50
60

Figure 7

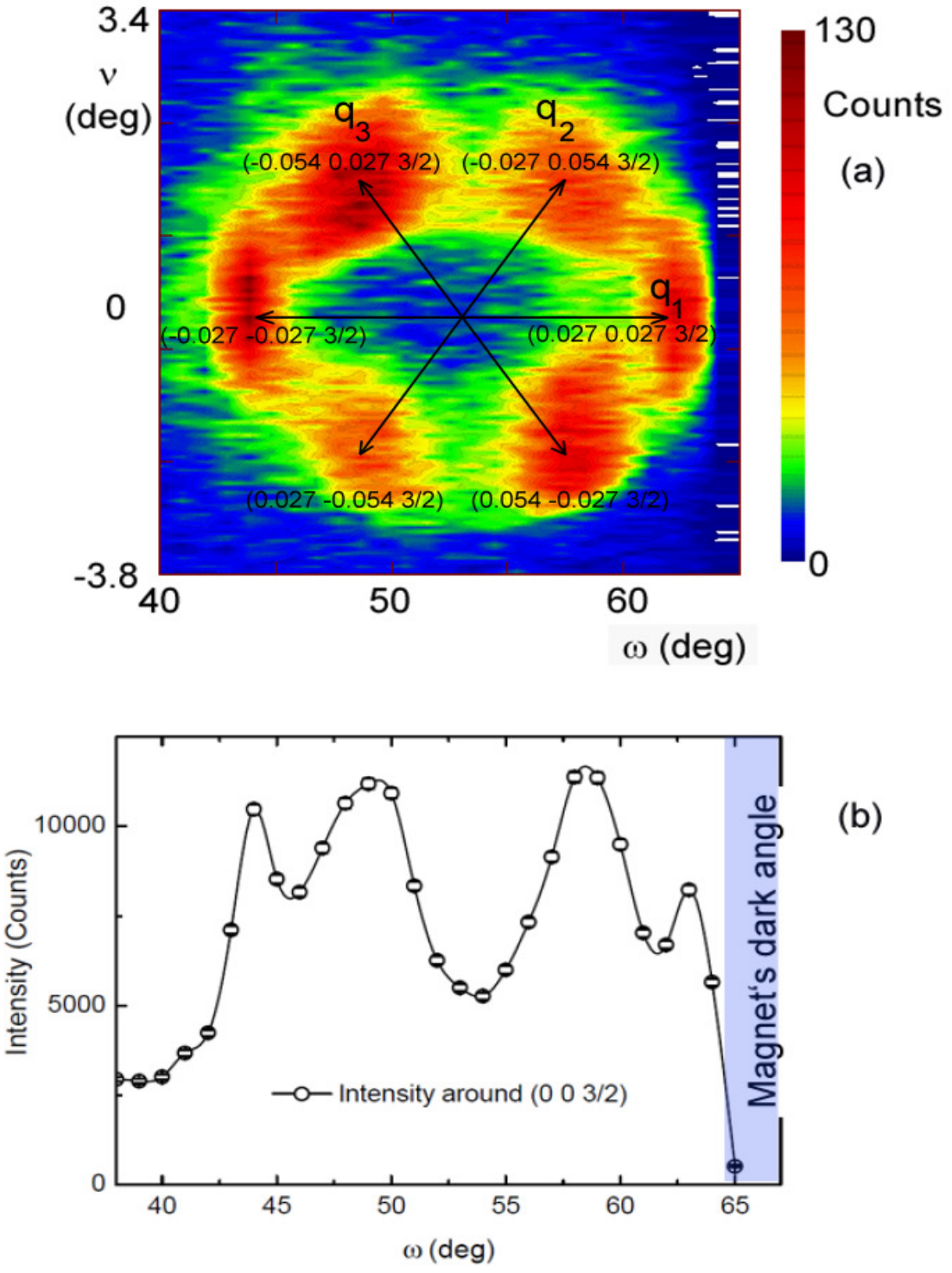
3.4
ν
(deg)
0
-3.8
40
50
60
ω (deg)
q3
(-0.054 0.027 3/2)
q2
(-0.027 0.054 3/2)
q1
(-0.027 -0.027 3/2)
(0.027 0.027 3/2)
(0.027 -0.054 3/2)
(0.054 -0.027 3/2)
130
Counts
0
(a)
Intensity (Counts)
10000
5000
0
40
45
50
55
60
65
ω (deg)
Intensity around (0 0 3/2)
Magnet's dark angle
(b)

Figure 8

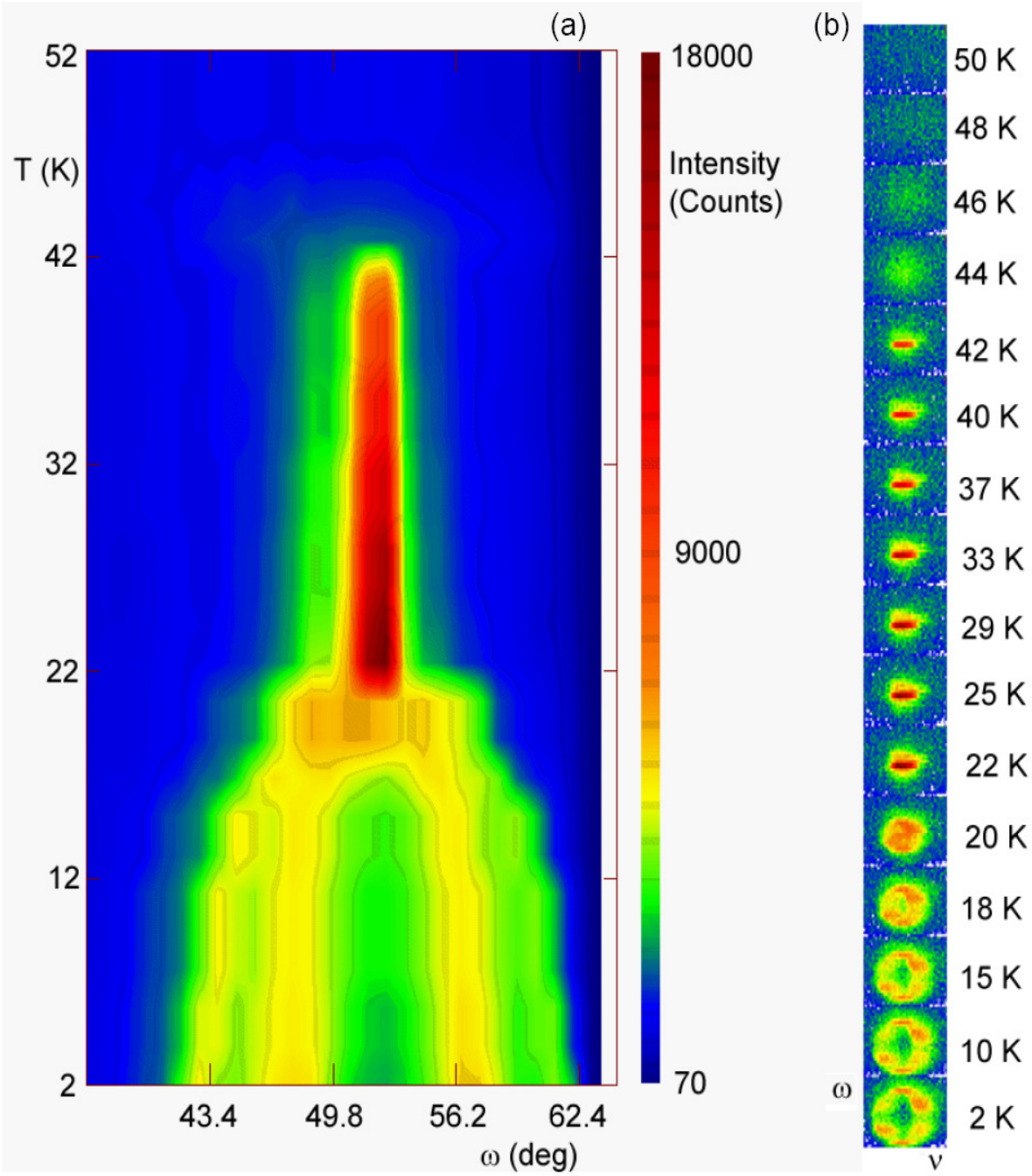
(a)
(b)
52
42
32
22
12
2
T (K)
43.4
49.8
56.2
62.4
ω (deg)
18000
Intensity
(Counts)
9000
70
50 K
48 K
46 K
44 K
42 K
40 K
37 K
33 K
29 K
25 K
22 K
20 K
18 K
15 K
10 K
2 K
ω
ν

Figure 9

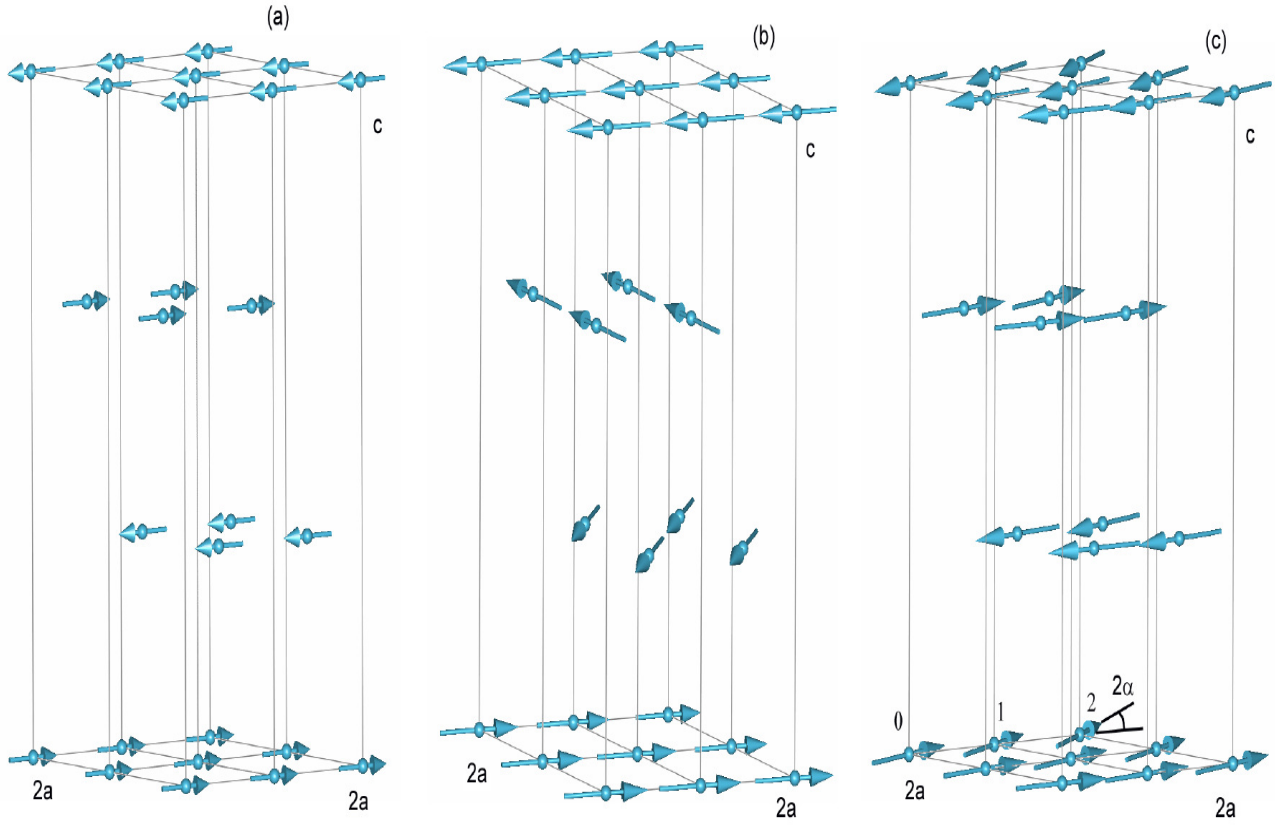

Figure 10

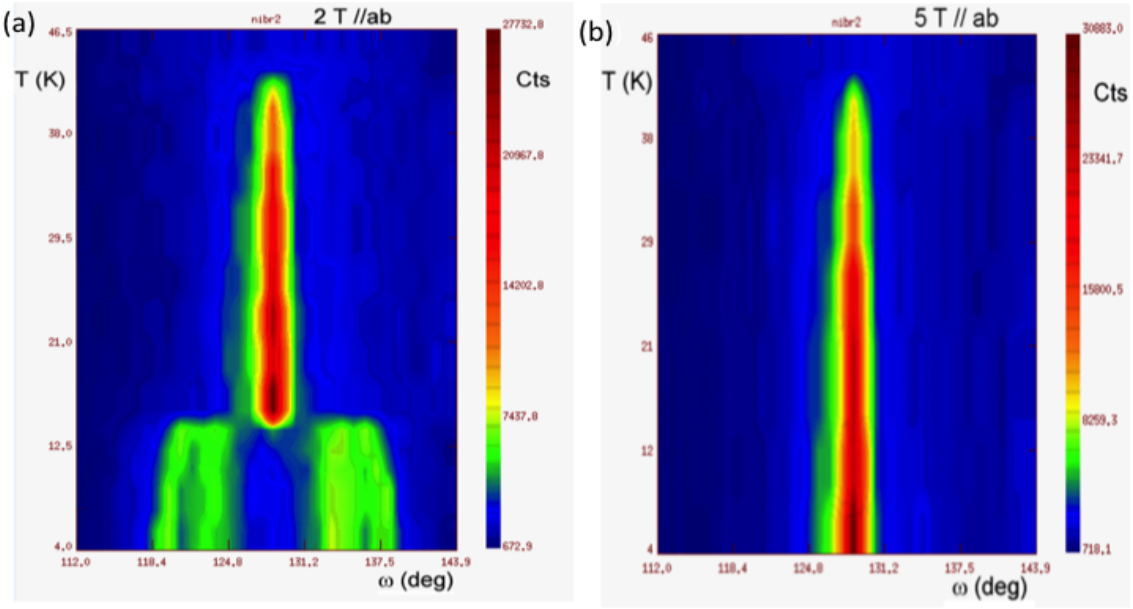

Figure 11

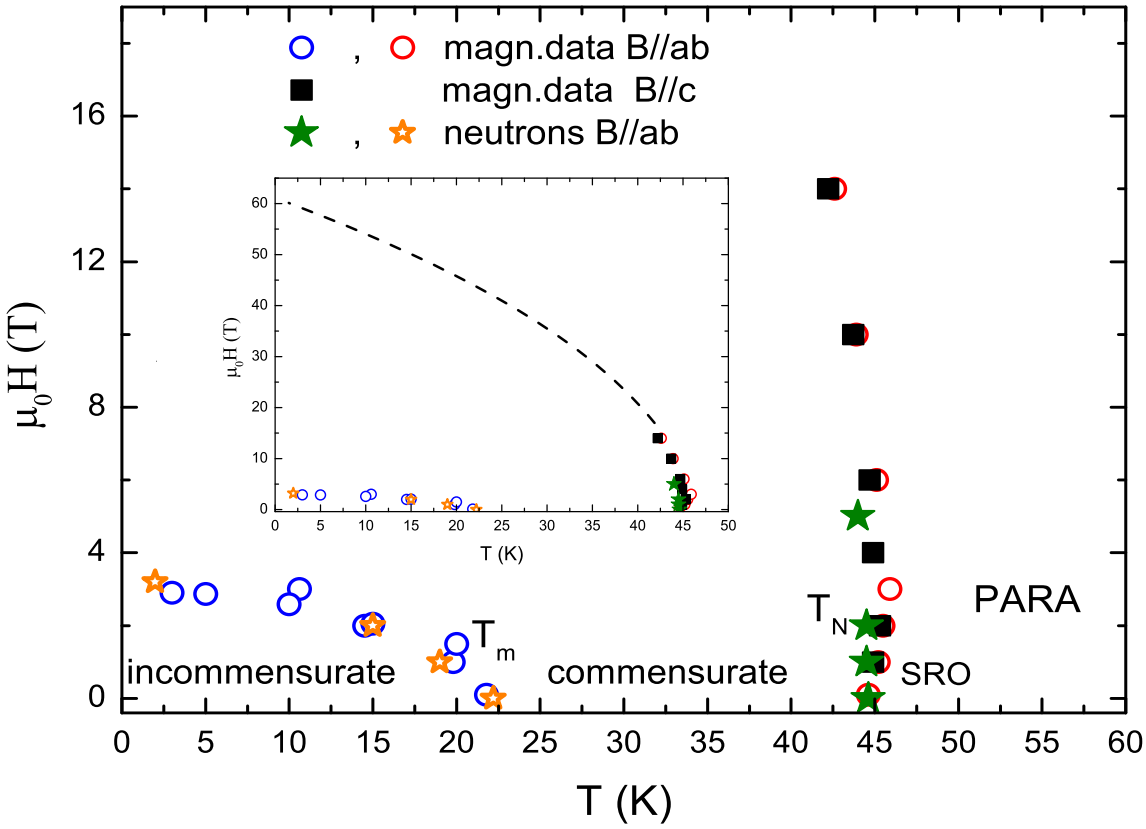
magn.data B//ab
magn.data B//c
neutrons B//ab
μ0H (T)
T (K)
T_m
T_N
incommensurate
commensurate
SRO
PARA